Acta Pharmaceutica Sinica B 2025;15(8):4210−4224

Chinese Pharmaceutical Association
Institute of Materia Medica, Chinese Academy of Medical Sciences

Acta Pharmaceutica Sinica B

www.elsevier.com/locate/apsb
www.sciencedirect.com

ORIGINAL ARTICLE

Dual-ferroptosis induction-based microneedle patches for enhanced chemodynamic/photothermal combination therapy against triple-negative breast cancer

Yujie Wang[a,†], Zhaoyou Chu[b,†], Peisan Wang[a,†], Tao Li[a], Yu Jin[a], Silong Wu[a], Xiaowei Song[c], Weinan Zhang[a], Miaomiao Yang[d], Zhengbao Zha[e], Haisheng Qian[a,f,g,*], Yan Ma[a,h,*]

[a]*School of Biomedical Engineering, Anhui Provincial Institute of Translational Medicine, Anhui Medical University, Hefei 230032, China*
[b]*Department of Critical Care Medicine, the First Affiliated Hospital of Anhui Medical University, Hefei 230032, China*
[c]*Department of Radiology, the First Affiliated Hospital of Anhui Medical University Research Center of Clinical Medical Imaging, Hefei 230032, China*
[d]*Department of Pathology, the First Affiliated Hospital of Anhui Medical University, Public Health Clinical Center, Hefei 230032, China*
[e]*School of Food and Biological Engineering, Hefei University of Technology, Hefei 230009, China*
[f]*Anhui Engineering Research Center for Medical Micro-Nano Devices, Anhui Medical University, Hefei 230011, China*
[g]*Institute of Health and Medicine, Hefei Comprehensive National Science Center, Hefei 230601, China*
[h]*Key Laboratory of Science and Engineering for the Multi-Modal Prevention and Control of Major Chronic Diseases, Ministry of Industry and Information Technology, Harbin Institute of Technology Zhengzhou Research Institute, Zhengzhou 450000, China*

Received 28 February 2025; received in revised form 18 April 2025; accepted 18 May 2025

*Corresponding authors.
E-mail addresses: shqian@ahmu.edu.cn (Haisheng Qian), may@ahmu.edu.cn (Yan Ma).
[†]These authors made equal contributions to this work.
Peer review under the responsibility of Chinese Pharmaceutical Association and Institute of Materia Medica, Chinese Academy of Medical Sciences.

https://doi.org/10.1016/j.apsb.2025.05.034

KEY WORDS

Triple-negative breast cancer;
Chemodynamic;
Ferroptosis;
Redox balance;
Lipid peroxides

Abstract Triple-negative breast cancer (TNBC) remains a refractory subtype of breast cancer due to its resistance to various therapeutic strategies. In this study, we introduce a "brake-release and accelerator-pressing" approach to engineer a microneedle patch embedded with copper-doped Prussian blue nanoparticles (Cu-PB) and the ferroptosis inducer sorafenib (SRF) for raised chemodynamic (CDT)/photothermal (PTT) combination therapy against TNBC. Upon transdermal insertion, the dissolving microneedles swiftly disintegrate and facilitate the release of SRF. Under gentle external light exposure, copper ions (Cu^{2+}) and iron ions (Fe^{3+}) were liberated from Cu-PB. The direct chelation of Cu^{2+} and the indirect suppression by SRF, collectively attenuate glutathione peroxidase 4 (GPX4) enzymatic function, destabilizing the cellular redox equilibrium (referred to as the "brake-release" strategy). The release of Cu^{2+} and Fe^{3+} ions instigates a Fenton/Fenton-like reaction within tumor cells, further yielding hydroxyl radicals and elevating reactive oxygen species (ROS) concentrations (referred to as the "accelerator-pressing" strategy). This overwhelming ROS accumulation, coupled with the impaired clearance of resultant lipid peroxides (LPO), ultimately triggers a robust ferroptosis cell death response. In summary, this study presents an innovative combinatorial therapeutic strategy based on dual-ferroptosis induction for TNBC, implying a promising therapeutic platform for developing ferroptosis-centered treatments for this aggressive breast cancer subtype.

1. Introduction

Triple-negative breast cancer (TNBC), defined by the lack of estrogen receptor (ER), progesterone receptor (PR), and human epidermal growth factor receptor 2 (HER2) expression, is currently regarded as an aggressive and unmanageable subtype of breast cancer[1]. Conventional treatments (surgical resection, chemotherapy, and radiotherapy) are often hampered by stubborn drug resistance, systemic toxicity, and suboptimal targeting specificity[2]. Ferroptosis, an iron-dependent form of programmed cell death distinct from apoptosis, necroptosis, and autophagy, is marked by the accumulation of lipid peroxidation (LPO) in the cell membrane and the reactive oxygen species (ROS), culminating in membrane rupture and cell death[3-7]. Consequently, ferroptosis emerges as a promising therapeutic strategy for various malignancies, given its independence from traditional molecular targets and the heightened susceptibility of drug-resistant cancer cells to this form of cell death[8].

In the process of ferroptosis, glutathione peroxidase 4 (GPX4) serves as a critical antioxidant enzyme essential for sustaining redox equilibrium by eliminating intracellular peroxides, particularly lipid peroxides[9-10]. Glutathione (GSH) is fundamental in the antioxidant defense system, reducing lipid peroxides and impeding the accumulation of ROS, thereby preventing ferroptosis[11]. Consequently, the induction of ferroptosis has shown promise in overcoming multidrug resistance in cancer[12]. Certain clinically approved pharmacological agents are pivotal in promoting ferroptosis in tumor cells, including RSL3, Erastin, and sorafenib (SRF)[13-15]. SRF has been evidenced to inhibit the cystine/glutamate antiporter (system Xc^- or xCT), a key element in ferroptosis, which leads to GSH depletion and GPX4 inactivation[16-17]. Nevertheless, the regulatory mechanisms governing ferroptosis are intricate, involving numerous signaling pathway interactions. Some pathways associated with ferroptosis may not be sufficiently activated by Sorafenib alone[18]. Furthermore, systemic administration can elicit severe adverse effects such as diarrhea, rash, and alopecia[19]. Therefore, it is imperative to explore innovative strategies dedicated to synergistic therapeutic regimens and precision delivery of ferroptosis-inducing agents[20].

Recent advancements have indicated that iron-based nanoparticles can trigger ferroptosis through the "iron pool effect" and Fenton reactions, establishing them as a promising class of ferroptosis inducers[21-22]. Notably, Prussian blue (PB), an antidote approved by the U.S. Food and Drug Administration (FDA) for thallium and other radioactive element poisoning, has demonstrated exceptional biosafety. The ferric (Fe^{3+}) and ferrous (Fe^{2+}) ions within PB can be released under external stimuli such as mild acidity and external light exposure, on account of the instability of the Fe−C ≡ N−Fe bond in acidic environments, positioning PB as a viable candidate for clinical applications in ferroptosis[23]. However, a large number of investigations have identified limitations including insufficient GSH depletion, inadequate drug delivery efficiency, and inflammatory responses triggered by excessive conventional photothermal therapy, which hinders the use of PB nanoparticles for ferroptosis treatment of tumors[24-26]. Moreover, it is reported that exogenous Cu^{2+} directly binds to the GPX4 protein, leading to its aggregation and subsequent autophagic degradation, thereby compromising its ability to eliminate excessive lipid peroxides, which accelerates the progression of ferroptosis[27-28]. Thus, combining copper/iron-based nanoparticles with clinical ferroptosis inducers could reduce the side effects of clinical drugs and effectively induce ferroptosis in tumor cells, potentially enhancing the efficacy of TNBC therapy.

Herein, we propose a "brake-release and accelerator-pressing" strategy to engineer a dissolving hyaluronic acid microneedle patch based on cascade ferroptosis, for the precise delivery of copper-doped Prussian blue nanoparticles (Cu-PB) and SRF to TNBC tissues. This dual induction approach for ferroptosis in tumor cells, facilitated by Cu-PB and SRF, is potentiated by mild photothermal therapy (PTT, $T \leq 42$ °C), which expedites the chemodynamic therapy (CDT) effect of Cu-PB, thereby significantly enhancing the therapeutic efficacy against TNBC. As depicted in Scheme 1, upon intradermal insertion, the microneedle rapidly dissolves, initiating the

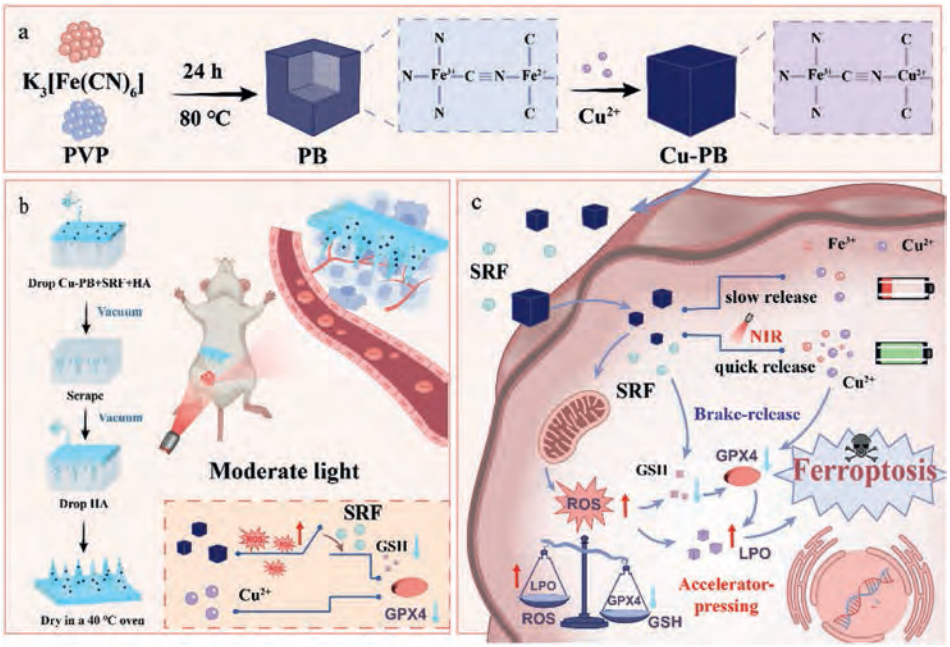

Scheme 1 Preparation of PB, Cu-PB, and Cu-PB + SRF@MNs and its application in treating triple-negative breast cancers. (A) The preparation of PB and Cu-PB nanoparticles. (B) The construction process of Cu-PB + SRF@MNs and treatment of mice. (C) Illustration of the tumor treatment of dual-ferroptosis induction by SRF and Cu-PB under mild near-infrared (NIR) laser irradiation.

release of SRF and Cu-PB nanoparticles, which liberates significant quantities of copper and iron ions within the tumor tissue under mild NIR laser irradiation. Cu^{2+} directly binds to GPX4, and SRF inhibits the cystine/glutamate antiporter (system Xc^- or xCT), synergistically impeding GPX4 functionality. This dual action induces ferroptosis in TNBC by "releasing the brake" on the intracellular antioxidant defenses. To efficiently induce ferroptosis, we also "press the accelerator" by ensuring ample "horsepower": Cu^{2+} and Fe^{3+} collaboratively act on H_2O_2 in TNBC, triggering a vigorous Fenton/Fenton-like reaction that generates highly cytotoxic hydroxyl radicals, further elevating ROS levels. Both aspects ultimately result in an accumulation of ROS and a pronounced increase in LPO. The "brake-release and accelerator-pressing" strategy robustly induces ferroptosis in tumor cells, ultimately achieving effective TNBC treatment. In conclusion, this work presents a promising therapeutic strategy for TNBC, based on a highly synergistic dual-ferroptosis induction paradigm.

2. Materials and methods

2.1. Materials

Hyaluronic acid (HA, molecular weight 20−40 kDa), cupric acetate monohydrate-($Cu(CH_3COOH)_2 \cdot H_2O$), hydrochloric acid (HCl), potassium ferricyanide ($K_3[Fe(CN)_6] \cdot 3H_2O$, 99.9%, *w/w*), ethanol and trisodium citrate dihydrate ($Na_3C_6H_5O_7 \cdot 2H_2O$) were procured from Shanghai Macklin Biochemical Co., Ltd. (Shanghai, China). Polyvinylpyrrolidone (PVP) and sorafenib (SRF) were acquired from Shanghai Aladdin Biochemical Technology Co., Ltd. (Shanghai, China). The Cell Counting Kit-8 (CCK-8) was obtained from Dojindo (Laboratories, Japan). The JC-1 staining kit and DCFH-DA were purchased from Biotium Biotechnology Co., Ltd. (Shanghai, China). BODIPY 581/591 C11 was attained from the Molecular Probes Master (Shanghai, China). Roswell Park Memorial Institute (RPMI) 1640 medium was acquired from Thermo Fisher Scientific, and penicillin/streptomycin and fetal bovine serum (FBS) were sourced from Invitrogen (MA, USA). Agar powder was bought from Solarbio (Beijing, China). Phosphate-buffered saline (PBS, pH = 6.5) was obtained from Gibco (Grand Island, USA). All reagents were of analytical grade and did not need further purification.

The crystallography of PB and Cu-PB was analyzed by X-ray diffractometer (Haoyuan Instrument Co., Ltd., DX-2700BH, Dandong, China). The size and potential of PB and Cu-PB were measured using nano-particle size and Zeta potential analyzer (Brookhaven Instruments, 90 Plus PALS, New York, NY, USA). The Microstereo Ultra High Precision Light Curing 3D Printer was used to print the microneedle patch (Boston Micro Fabrication, S130, Shenzhen, China). The preparation of microneedles was characterized by scanning electron microscopy (Guoyi Quantum Hefei Technology Co., Ltd., SEM3100, Hefei, China), ultra-depth-of-field three-dimensional microscopy (Motic China Group Co., Ltd., Easyzoom, Xiamen, China), and optical cameras. A Coupled Plasma Mass Spectrometer was used for quantitative analysis of the total copper and iron contents from different samples and organs (Hangzhou Puyu Technology Development Co., Ltd., EXPEC 6500, Hangzhou, China). Flow cytometric analysis for cells was performed by multicolor analytical flow cytometry (Beckman Coulter Co., Ltd., CytoFLEX, Shanghai, China). CCK-8 and Kit detection analysis was performed using the multifunctional microplate reader (Meigu Molecular Instruments (Shanghai) Co., Ltd., SpectraMax iD3, Shanghai, China). Cell staining and 3D microneedle scanning were performed using the laser confocal microscopy imaging system (Beijing Century Sunny Technology Co., Ltd., CSIM-130, Beijing, China). Blood routine tests were performed on mice using an

automated blood cell analyzer (Mindray Animal Care Co., Ltd., BC-5000VET, Shenzhen, China).

2.2. Preparation of Prussian blue (PB) and copper-doped Prussian blue nanoparticles (Cu-PB)

Preparation of PB: To prepare the PB solution, dissolve 1584 mg of $K_3[Fe(CN)_6]\cdot 3H_2O$ and 36 g of PVP in 360 mL of deionized water. 300 mL of concentrated HCl was added to the solution, which was then stirred for 1 h. The mixture was heated, washed, and freeze-dried and the nanoparticles were stored at room temperature.

Preparation of Cu-PB: PB (20 mg) was dissolved in 8 mL of water containing $Na_3C_6H_5O_7\cdot 2H_2O$ (27 mg), followed by the addition of PVP, which was sonicated until fully dissolved. Cu $(CH_3COOH)_2\cdot H_2O$ (8.8 mg) was then added and stirred at room temperature for 24 h, after which the mixture was washed with deionized water and anhydrous ethanol, freeze-dried and stored.

2.3. Preparation of MN patches

A mixture of 28 mg Cu-PB, 7 mg SRF, and 100 mg HA (molecular weight 2×10^5−4×10^5) was dissolved in 2 mL DI water and stirred overnight. The solution was injected into a 3D-printed microneedle mold and vacuum-treated for three cycles until the micropores were filled. The mold was then dried overnight at 40 °C to obtain Cu-PB + SRF@MNs[19].

2.4. Characterization of copper-doped prussian blue nanoparticles (Cu-PB)

The surface morphology and optical properties of the materials were analyzed using TEM, SEM, XRD, and XPS. The release of metal ions from the nanoparticles was quantified using ICP-MS.

2.5. Characterization of MN patches

The morphology of the microneedle patches was examined using SEM and super-depth microscopy for layer-by-layer scanning. 3D internal imaging was performed with laser CSIM. Mechanical properties were assessed using an electronic universal testing machine. The microneedles were placed on a steel plate, and a probe detector was moved vertically at 0.5 mm/min with a maximum load of 50 N. Force-displacement curves were recorded at the point of fracture of the tip or substrate.

2.6. Evaluation of catalytic activity of Cu-PB in vitro

The catalytic activity of Cu-PB in the presence of H_2O_2 was evaluated using TMB, OPD, and DTNB, with absorbance measured by UV−Visible spectrophotometry.

2.7. Cytotoxicity measurements

The cytotoxicity of Cu-PB on L929, HUVECs and 4T1 cells was evaluated using the CCK-8 assay, where 4T1 cells (1×10^4 cells/well) were treated with different concentrations of Cu-PB (0, 6.25, 12.5, 25, 50, 75, 100, 125, 150 and 200 μg/mL) for 4 h, irradiated with an 808 nm laser and incubated for 20 h, followed by the addition of CCK-8 reagent and measurement of absorbance at 450 nm to determine cell viability.

2.8. Detection of intracellular ROS production

4T1 cells were cultured for 20 h in confocal petri dishes at a density of 1×10^5 cells per dish until the fusion degree reached about 60%. During the final 4 h, cells were treated with nanoparticles. The experimental group was subjected to irradiation with an 808 nm laser. Following irradiation, DCFH-DA was added for 30 min. After two washes with buffer, images were captured using CLSM to assess the levels of ROS.

2.9. Cell viability test

4T1 cells (1×10^5 cells/dish) were seeded in confocal dishes and incubated for 24 h to reach approximately 80% confluence. After 12 h of nanoparticle exposure, the cells were stained with Calcein-AM (50 μL, 0.02 mol/L) and PI (50 μL, 0.02 mol/L) and observed using CLSM.

2.10. Detection of cellular ferroptosis

Overnight, 4T1 cells were cultured in confocal dishes at 1×10^5 cells/dishes, resulting in about 60% fusion. The cells were then treated with nanoparticles for 4 h. Following treatment, the cells were incubated in the dark with BODIPY 581/591 C11 (20 μL, 0.02 mol/L) in a cell culture incubator. This dye binds to lipids and exhibits green fluorescence (λ_{ex} = 500 nm, λ_{em} = 510 nm). After 30 min of incubation, the cells were imaged using CLSM to evaluate the potential for cellular ferroptosis.

2.11. Animal therapy experiments

All experimental procedures were executed according to the protocols approved by the Anhui Medical University Animal Care and Use Committee. Once tumors reached a volume of 50−80 mm^3, mice bearing orthotopic breast cancer were randomly assigned to eight groups (n=5). Treatment was administered by applying microneedles to the tumor for 5 min. For groups requiring light irradiation, mice were anesthetized and irradiated with an NIR laser (1 W/cm^2, 5 min). Tumor site temperature was monitored using an IR thermal imager ($T \leq 42$ °C) and tumor volume ($V = l \times w^2/2$) and body weight were measured to assess tumor growth. Small animal imaging was conducted using D-fluorescein sodium at 5-day intervals for 25 days. Mice were euthanized when tumor volume reached 1300−1500 mm^3.

2.12. Animal therapeutic slice experiments

Female BALB/c mice were implanted with tumors and randomly assigned to eight groups (n=5). Treatment was administered *via* microneedles targeting the tumor for 5 min. Mice requiring light irradiation were anesthetized and treated with NIR laser (1 W/cm^2, 5 min), then euthanized on Day 15 for tumor tissue removal and H&E, TUNEL, Ki67, GPX4, and DHE staining, along with histological analysis of major organs.

2.13. Statistical analysis

The data were considered statistically significant based on one-way ANOVA analysis. Representative experimental results are expressed as the mean ± standard deviation (SD). The threshold

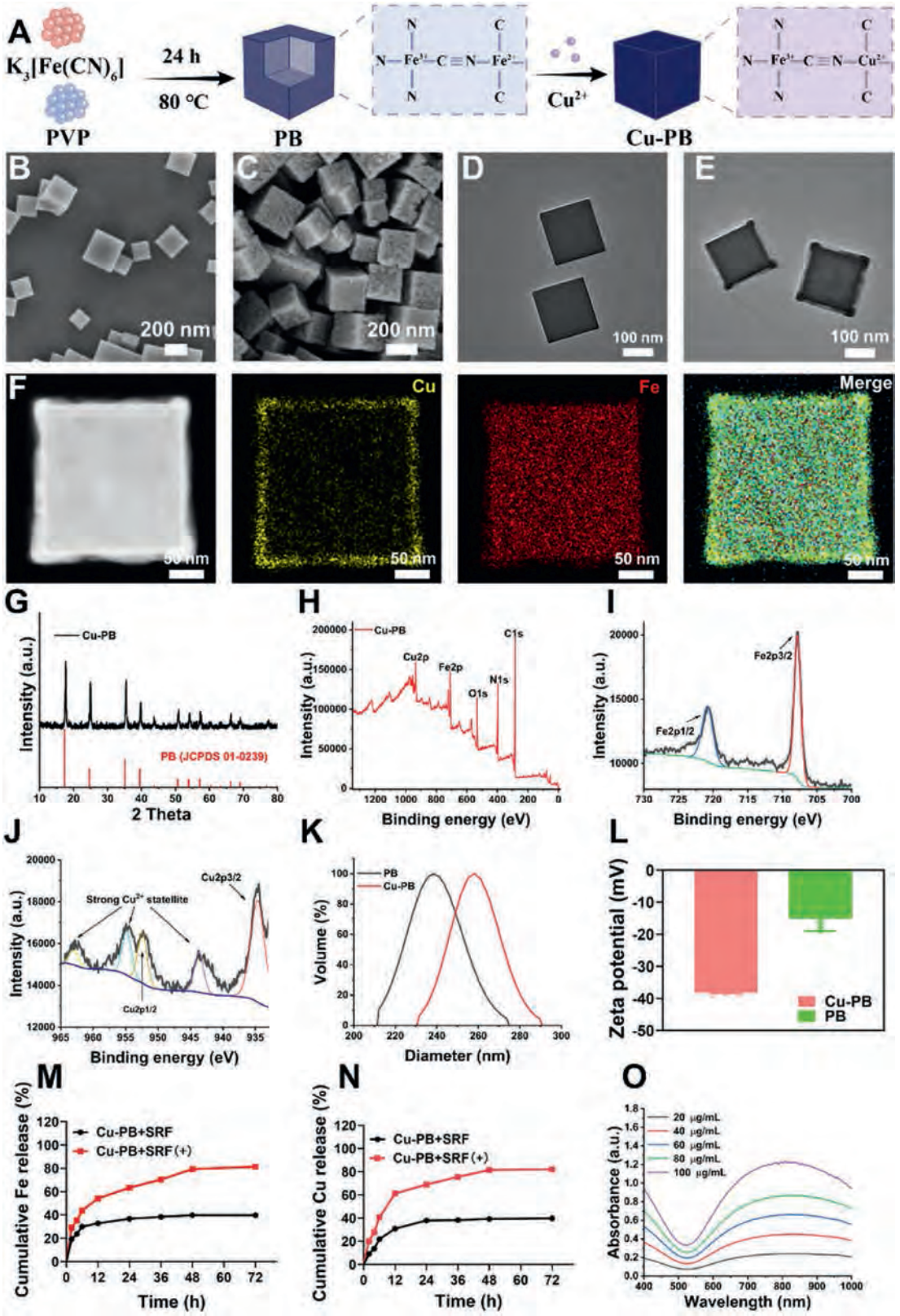

Figure 1 Preparation, characterization, and performance testing of PB and Cu-PB. (A) The preparation procedure of PB and Cu-PB. (B, C) SEM images of PB (B), Cu-PB (C). Scale bar = 200 nm. (D, E) TEM images of PB (D), Cu-PB (E). Scale bar = 100 nm. (F) Dark-field and the merged image of Cu-PB and elemental maps of Cu, Fe. Scale bar = 50 nm. (G) XRD plots of Cu-PB. (H−J) XPS analysis of Cu-PB. (K) The particle size of PB, Cu-PB. (L) Changes in zeta potentials of PB and Cu-PB. (M, N) Accumulation of degraded Cu-ions and Fe-ions from Cu-PB immersed in PBS at different temperatures. (O) UV−Vis−NIR spectra of Cu-PB.

for statistical significance was set at $*P < 0.05$, with specific significance levels indicated as follows: $**P < 0.01$; $***P < 0.001$; $****P < 0.0001$.

3. Results and discussion

3.1. Synthesis and characterization of PB and Cu-PB

PB and Cu-PB were synthesized as depicted in Fig. 1A[29]. Transmission electron microscopy (TEM) and scanning electron microscopy (SEM) analyses revealed that the synthesized PB and Cu-PB possessed relatively homogeneous sizes and were monodisperse (Fig. 1B−E). To verify the successful incorporation of Cu ions into PB *via* ion exchange, elemental mapping was employed (Fig. 1F). The results confirmed the homogeneous incorporation of Cu ions into PB, forming a "core−shell structure". The Cu to Fe mass fraction in Cu-PB was determined to be 64.2% by inductively coupled plasma optical emission spectrometry (ICP-OES, Supporting Information Table S1). As illustrated in Fig. 1G, no discernible novel characteristic peaks were identified in Cu-PB, indicating that Cu ions doping did not alter the inherent PB phase (JCPDS 01−0239). X-ray photoelectron spectroscopy (XPS) analysis further confirmed the chemical composition of Cu-PB, identifying the presence of C, O, N, Cu, and Fe (Fig. 1H and I). The survey spectrum revealed the presence of Cu^{2+} sharp characteristic satellites at 944, 955, and 962.5 eV, corroborating the successful synthesis of Cu-PB and the oxidation state of the doped Cu ions as Cu^{2+} (Fig. 1J). Fig. 1K illustrates that the average hydrated particle size of PB and Cu-PB was 248 ± 0.8 and 256 ± 0.8 nm, respectively. Zeta potential measurements showed a shift in surface charge from −15 to −38 mV upon Cu^{2+} incorporation into PB (Fig. 1L). As previously reported in the literature, mild NIR laser irradiation promoted the rapid dissociation of Cu−C ≡ N−Fe bonds, facilitating the release of Fe and Cu ions from Cu−PB[30]. As shown in Fig. 1M and N, a significant increase in the detection of copper and iron ions was observed using ICP-MS at elevated temperatures over various time intervals in PBS buffer. Under light exposure, Cu and Fe ion release reached 82% and 81% at 72 h, respectively, which was substantially higher than without light exposure, indicating a rapid release upon irradiation. The UV−Vis−NIR spectra revealed that Cu-PB exhibited minimal change in the peak compared to PB at 808 nm (Supporting Information Fig. S1) and the absorption peaks in the NIR window increased with higher Cu-PB concentrations (Fig. 1O), manifesting the enormous potential of Cu-PB as a mild photothermal reagent.

3.2. Preparation and characterization of MN

Fig. 2A illustrates the principal fabrication process of Cu-PB + SRF@MNs[19,33]. A composite solution of HA, Cu−PB, and SRF was introduced into the microneedle mold, subjected to vacuum treatment thrice to eliminate air bubbles, sealed with a PVP aqueous solution, and subsequently dried to yield the Cu-PB + SRF@MNs. The resultant Cu-PB + SRF@MNs patch array consists of 12 × 12 needles, with a height of 1000 μm and a width of 200 μm at the base, manifesting uniformly sharp, neatly aligned tips and a complete pyramidal shape as confirmed by the optical camera, SEM images and ultra-depth microscope images (Fig. 2B−E). Nile Red dye served as a model drug, integrated into the microneedles, and 3D fluorescence images were obtained by layer-by-layer scanning using confocal laser scanning microscopy (CLSM), demonstrating homogeneous drug distribution at the microneedle tips (Fig. 2F and G). The mechanical properties of Cu-PB + SRF@MNs and HA@MNs were evaluated using a universal testing machine to assess their skin penetration capabilities, with the result that Cu-PB + SRF@MNs suggested flexibility without fracturing under compression, as reflected in Supporting Information Fig. S2.

Subsequently, methylene blue (MB)-filled Cu-PB + SRF@MNs were fabricated to assess their skin penetration, dissolution behavior, and adhesion to the skin surface. Fig. 2H and I illustrate that the microneedle patch exhibited robust adhesion to the skin in both vertical and inverse orientations, with the microneedles dissolving completely within 10 min, revealing excellent dissolvability. The force-displacement analysis revealed that the insertion force for HA@MNs was approximately 10 ± 0.5 N at a 300 μm displacement, whereas Cu-PB + SRF@MNs exhibited a significantly increased insertion force of 24 ± 0.5 N under the same displacement (Fig. 2J), indicating enhanced mechanical strength due to the Cu-PB and SRF blend[31]. Post removal of the Cu-PB + SRF@MN patch, a well-ordered array of micropores was observed on the mouse skin, which healed within 60 min, and the mice displayed normal behavior within 24 h, signifying favorable biocompatibility for Cu-PB + SRF@MN patches (Fig. 2K). The punctured mouse skin was then incised and stained with hematoxylin and eosin (H&E) to visualize the pinholes under an optical microscope (Fig. 2L), where the pinholes were distinctly observable. The MB-containing microneedles were embedded in agarose to evaluate the SRF release capabilities, with the samples divided into two groups: one exposed to a NIR laser (808 nm) for 5 min and the other maintained at room temperature for 60 min (Supporting Information Figs. S3 and S4). Notably, the laser-irradiated group illustrated a substantial increase in methylene blue release, demonstrating enhanced drug penetration and diffusion. These results corroborate the hypothesis that the microneedle patch can achieve thermally enhanced drug release.

3.3. Photothermal and catalytic properties in vitro

The thermal properties of the Cu-PB solution (100 μg/mL) escalated in correlation with an increase in laser power density, reaching 45 ± 1 °C after 5-min 808 nm laser exposure at 1 W/cm^2 power density (Fig. 3A). The temperature variations of Cu-PB solutions at varying concentrations were assessed under the same laser power conditions (Fig. 3B). Under similar irradiation, DI water experienced a temperature increase of 4.6 ± 0.5 °C. With an escalation in solution concentration, the Cu-PB solution's temperature demonstrated a significant rise, with higher concentrations correlating to a more pronounced thermal increase. Subsequent NIR irradiation (1 W/cm^2, 8 min) over five cycles on Cu-PB samples revealed sustained peak temperatures, indicative of superior photothermal stability (Fig. 3C). Infrared (IR) thermal imaging validated the photothermal conversion capabilities of Cu-PB (Supporting Information Fig. S5), with a notable photothermal conversion efficiency (η) reaching 34% at 808 nm (Fig. 3D). Based on the inherent photothermal advantages, Cu-PB nanoparticles were incorporated in Cu-PB + SRF@MNs, endowing them with superior photothermal performance and stability compared to HA@MNs (Supporting Information Fig. S6 and

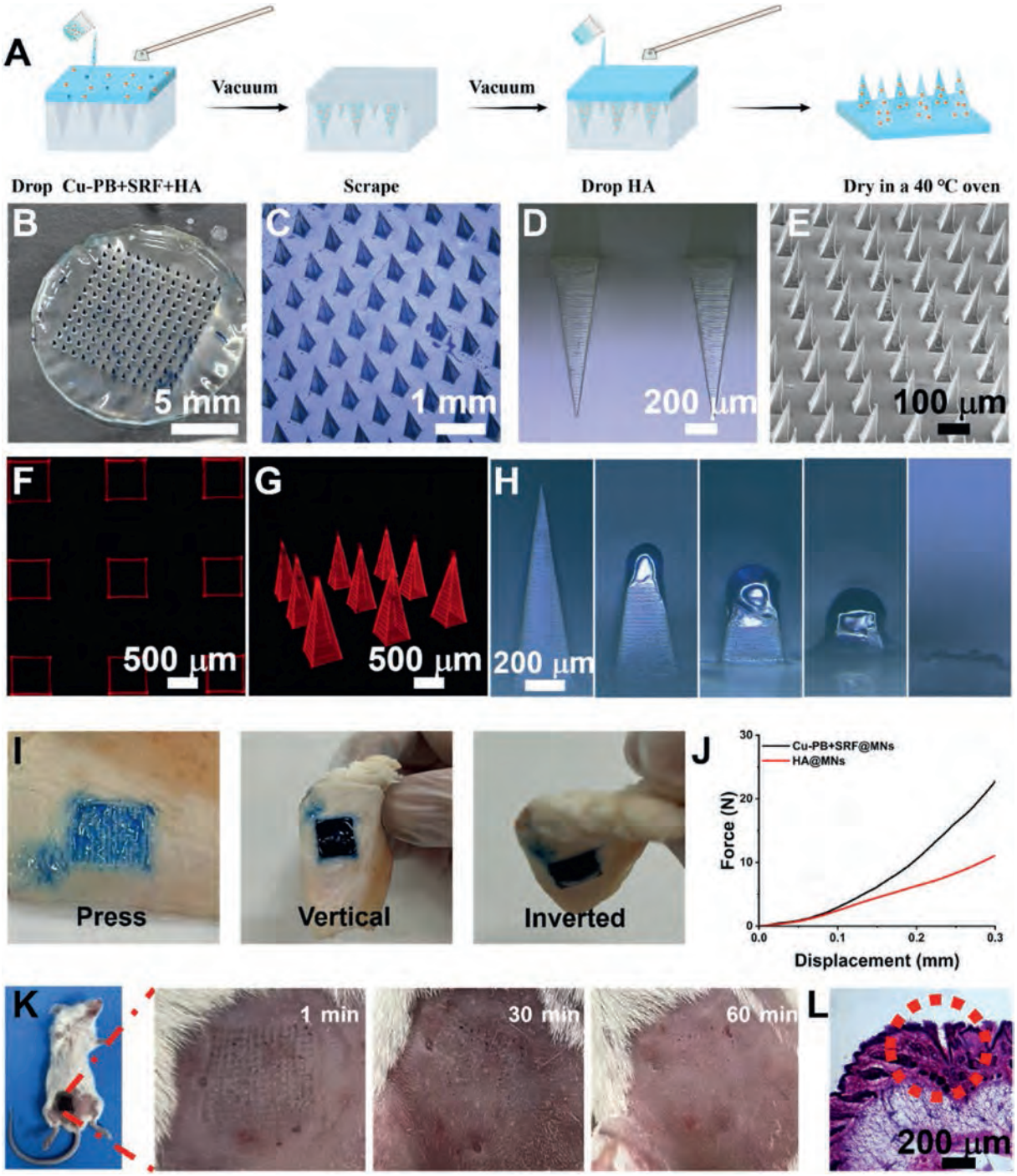

Figure 2 Preparation and characterization of Cu-PB + SRF@MNs. (A) Flow chart of the synthesis and preparation of Cu-PB + SRF@MNs. (B) Optical photograph. Scale bar = 5 mm, (C, D) depth-of-field microscope images (scale bar = 1 mm and scale bar = 200 μm), and (E) SEM images of Cu-PB + SRF@MNs. Scale bar = 100 μm. (F, G) 3D fluorescence images of MN. Scale bar = 500 μm. (H) Dissolution experiment of Cu-PB@MNs. Scale bar = 200 μm. (I) Pigskin pressing experiments of Cu-PB@MNs. (J) Mechanical strength of MNs. (K) Mouse skin puncture test of Cu-PB + SRF@MNs. (L) H&E picture of Cu-PB + SRF@MNs puncture. Scale bar = 200 μm.

Fig. 3E). The reactive oxygen species (ROS) generation ability of Cu-PB was assessed through chemical probes, including 3,3′,5,5′-tetramethylbenzidine (TMB) and *o*-phenylenediamine (OPD). Similar to the literature, an increase in ROS production coinciding with higher Cu-PB concentrations was ascribed to the swift cleavage of Cu−C ≡ N−Fe bonds during mild NIR laser irradiation, promoting the release of Fe^{3+} and Cu^{2+}, thereby augmenting ROS generation (Fig. 3F−I)[32]. A quantitative analysis of the UV absorption curves at varying drug mass concentrations affirmed SRF release from Cu-PB + SRF@MNs, depicting a robust linear association between drug concentration and absorbance (Supporting Information Fig. S7). Consistent with the preceding approach, drug release experiments were conducted utilizing the fabricated Cu-PB + SRF@MNs, with drug release

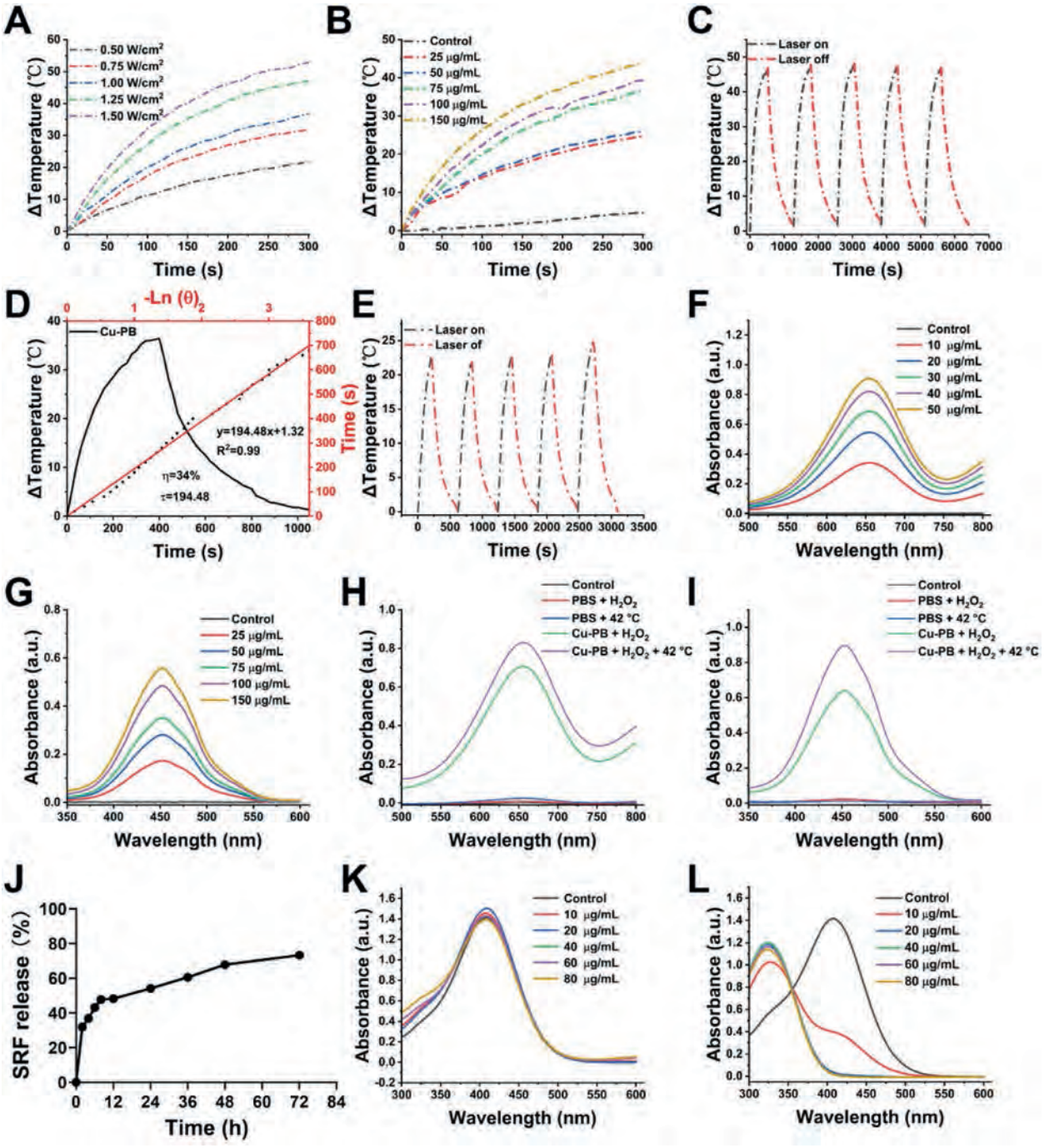

Figure 3 Photothermal and catalytic performances *in vitro*. Temperature variation curves of Cu-PB solution under 808 nm NIR laser irradiation (A) at varying power densities and (B) concentrations. (C) Temperature curves of heating and cooling cycles of Cu-PB solution under 808 nm laser irradiation. (D) Photothermal conversion efficiency (η) and thermal conversion constant (τ) of Cu-PB. (E) Temperature curves of heating and cooling cycles of Cu-PB + SRF@MNs under 808 nm laser irradiation. (F—I) Changes in the absorbance of TMB and OPD upon adding H_2O_2 to Cu-PB at different concentrations and under various conditions. (J) Release curves of SRF. (K, L) *In vitro*, depletion of reduced GSH by PB and Cu-PB at varying concentrations was quantified using DTNB absorbance.

monitored and quantified at various intervals, as depicted in Fig. 3J. It is worth noting that Cu-PB exhibited significant GSH depletion properties, outperforming PB under weakly acidic conditions (Fig. 3K and L). The findings underscored the exceptional photothermal conversion ability and catalytic activity of Cu-PB *in vitro*.

3.4. Cellular uptake and cytotoxicity activities of Cu-PB

The cellular uptake and cytotoxicity profiles of Cu-PB were comprehensively evaluated *in vitro*. The intracellular red fluorescence from Nile Red-labeled Cu-PB was monitored at various time intervals using CLSM images (Fig. 4A), while bio-

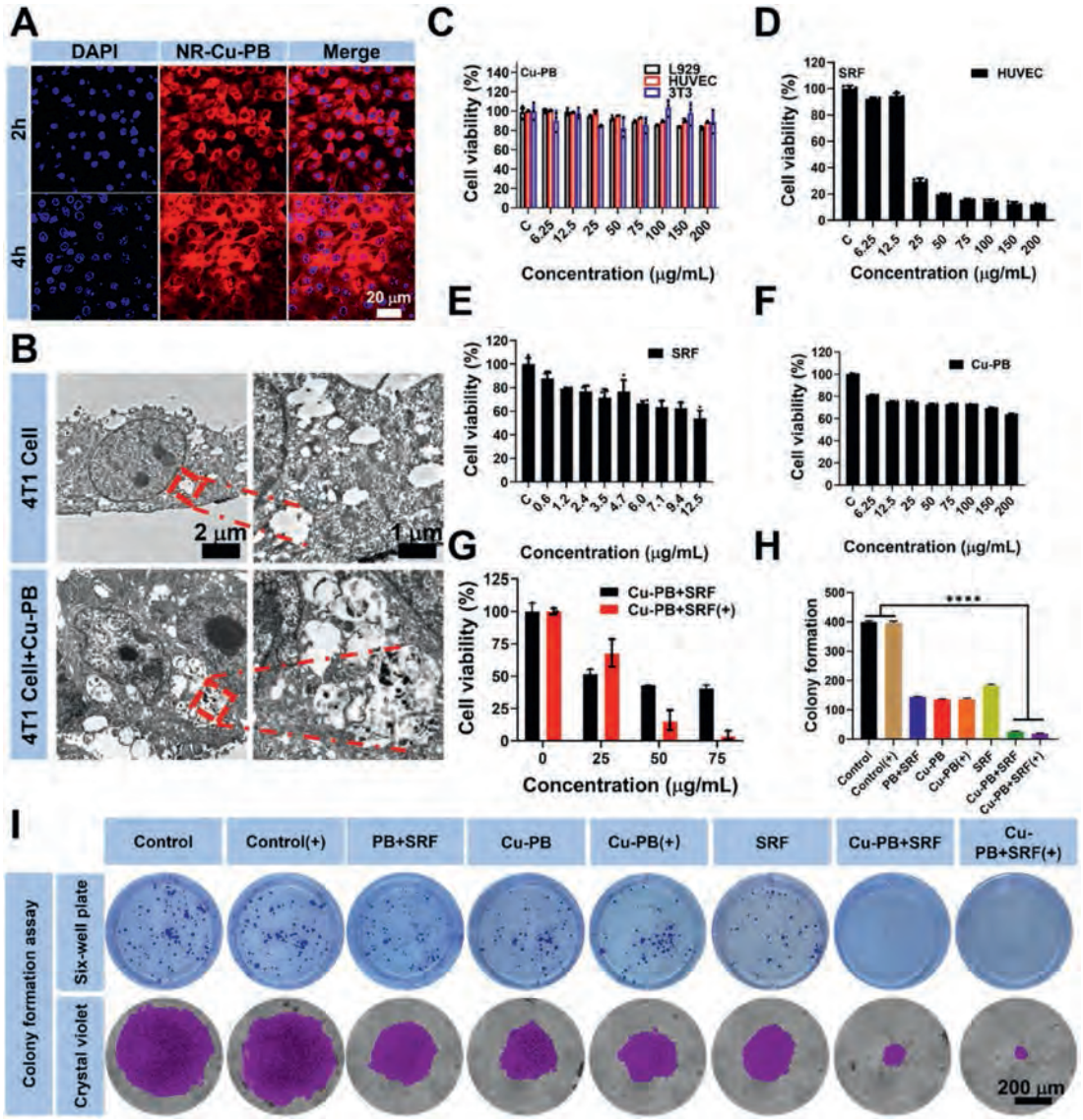

Figure 4 *In vitro* evaluation of the therapeutic effect of Cu-PB. (A) CLSM images of 4T1 cells co-cultured with Cu-PB. Scale bar = 20 μm. (B) Bio-TEM image of 4T1 cells incubated with Cu-PB for 24 h. Scale bar = 2 μm and scale bar = 1 μm. (C) Relative cell viability of L929 cells, HUVEC cells, and 3T3 cells after 24 h incubation with Cu-PB. (D) Relative cell viability of HUVEC cells after 24 h incubation with SRF. (E, F) The effect of varying concentrations of Cu-PB and SRF on the viability of 4T1 cells was investigated. (G) The cell viability of 4T1 cells treated with Cu-PB and SRF under different conditions. (H, I) Analysis of proliferation in each group after incubation with 4T1 cells and quantitative. Scale bar = 200 μm. Data are presented as mean ± SD (n = 3). ****$P < 0.0001$.

electronic microscopy (Bio-TEM) images (Fig. 4B) revealed its internalization into cytoplasmic vesicles post co-incubation with 4T1 cells, thereby confirming the effective uptake of Cu-PB by these cells. The biocompatibility of Cu-PB was assessed using the Cell Counting Kit-8 (CCK-8) assay with results indicating that survival rates of L929, HUVEC and 3T3 cells remained above 80% at Cu-PB concentrations up to 200 μg/mL, suggesting favorable biocompatibility of Cu-PB, while the safe concentration range for SRF in normal cells was established to be 0−12.5 μg/mL (Fig. 4C and D). At the same time, the cytotoxicity of Cu-PB at varying concentrations (both before and after light exposure) to normal cells was also evaluated (Supporting Information Fig. S8). The findings implied that different concentrations of Cu-PB, regardless of light exposure, did not lead to cell death under standard physiological conditions. Sequential viability assessments of 4T1 cells treated with Cu-PB, SRF, and Cu-PB + SRF (−/+), revealed that cell mortality increased with higher concentrations of both agents after 12 h of co-culturing (Fig. 4E and F). Notably, the cell-killing efficiency reached up to 97% due to the synergistic effect of Cu-PB and SRF, especially under mild NIR laser irradiation (Fig. 4G). Building upon previous ion release studies, we examined the impact of ions (Cu^{2+} and Fe^{3+}) released from Cu-PB on cytotoxicity toward normal cell lines, showing that the equivalent concentrations of Cu^{2+} and Fe^{3+} ions had minimal toxicity to normal cells (Supporting Information Figs. S9 and S10). Additionally, cell scratch and colony formation assays indicated superior inhibitory effects in the Cu-PB + SRF (+) group compared to other groups

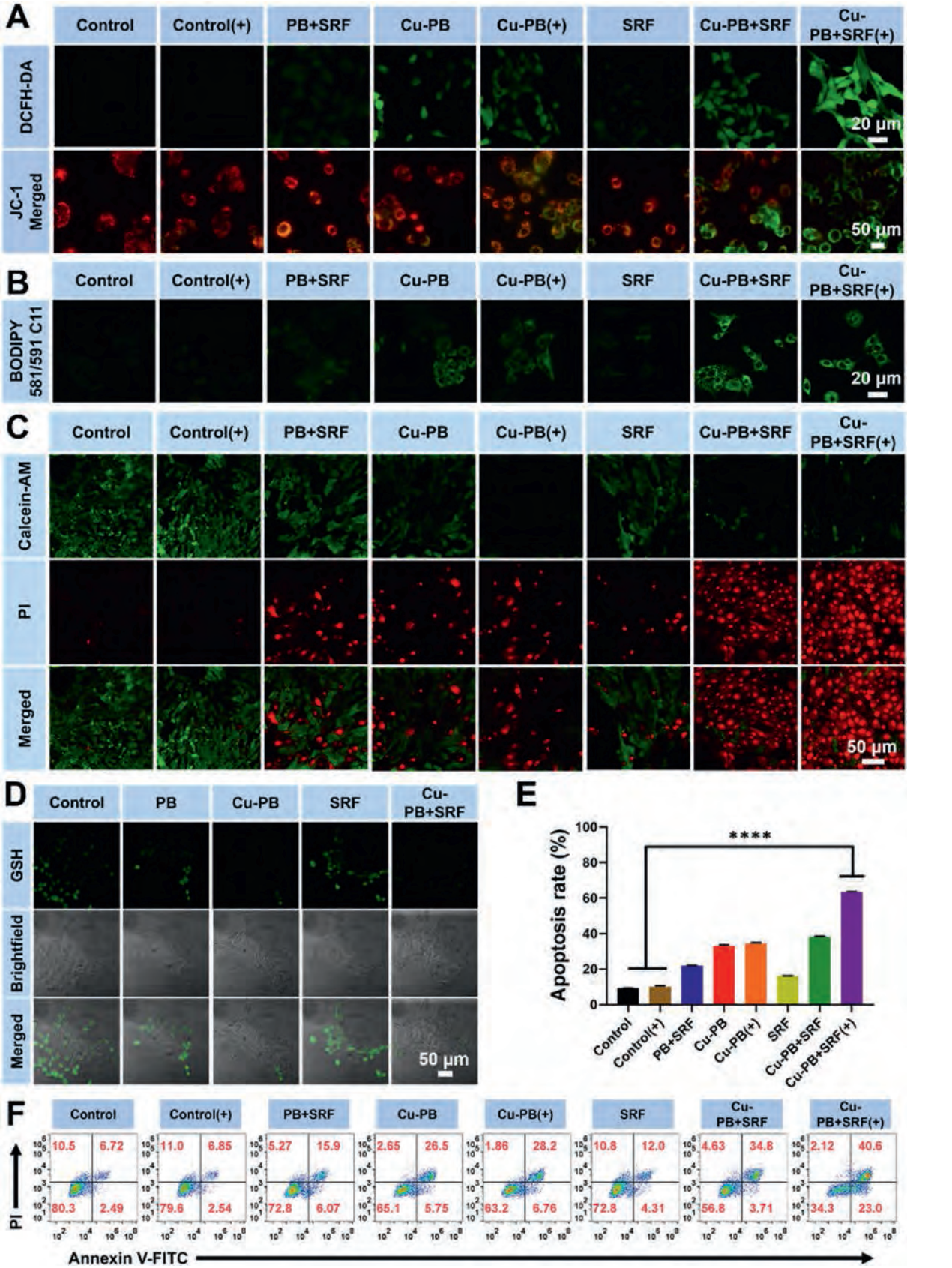

Figure 5 *In vitro* therapy effect of Cu-PB. (A) CLSM images of 4T1 cells to detect the ROS level and the mitochondrial membrane potential damage. Scale bar = 20 μm and scale bar = 50 μm. (B) BODIPY581/591-C11 staining CLSM images of 4T1 cells to detect lipid peroxidation. Scale bar = 20 μm. (C) Cytotoxicity profiles of 4T1 cells treated with different groups by Calcein-AM/PI double staining. Scale bar = 50 μm. (D) CLSM images of 4T1 cells for GSH levels. Scale bar = 50 μm. (E, F) Flow cytometric analysis of 4T1 cells subjected to different groups. Data are presented as mean ± SD ($n = 3$). ****$P < 0.0001$.

(Fig. 4H and I, Supporting Information Fig. S11). These results highlighted that Cu-PB could be effectively internalized by tumor cells and, in conjunction with SRF, could exert potent cytotoxic effects *in vivo* under mild laser irradiation.

3.5. Intracellular catalytic activity and induction of ferroptosis of Cu-PB

To evaluate the efficacy of Cu-PB in generating ROS, intracellular ROS levels were assessed using the 2′,7′-dichloro-fluorescein diacetate (DCFH-DA). As illustrated in Fig. 5A (top), the Cu-PB + SRF group showed significantly enhanced green fluorescence, particularly under mild NIR laser irradiation, indicating augmented ROS generation due to the thermal effect (Supporting Information Fig. S12). Mitochondrial impairment was assessed *via* 5,5′,6,6′-tetrachloro-1,1′,3,3′-tetraethylbenzimidazolyl carbonyl anthocyanin iodide (JC-1) staining. Fig. 5A (bottom) showed intense red fluorescence in the control and control (+) groups, whereas the Cu-PB + SRF (+) group exhibited prominent green fluorescence, suggesting substantial oxidative stress and consequent mitochondrial damage induced by the Cu-PB, SRF, and mild NIR laser combination. Elevated intracellular ROS levels are predictive of increased LPO, with the ferroptosis cell death process relying on the intracellular accumulation of LPO. Fig. 5B illustrates that CLSM using BODIPY 581/591 C11 (green fluorescence) detected a pronounced accumulation of green fluorescence in 4T1 cell membranes treated with Cu-PB + SRF (+) under 808 nm laser irradiation, confirming effective ferroptosis induction by lipid peroxidation in tumor cells (Supporting Information Fig. S13). These results could be attributed to Fenton/Fenton-like reactions involving Fe^{3+} and Cu^{2+} ions indirectly enhancing lipid peroxidation by generating ROS, such as ·OH. To further explore the synergistic cytotoxic effects of Cu-PB + SRF (+), a live/dead assay was conducted on 4T1 cells using Calcein-AM and PI staining. The control and control (+) groups predominantly exhibited green fluorescence, indicating minimal cell death, whereas the Cu-PB + SRF (+) group displayed strong red fluorescence, denoting a higher extent of cell death (Fig. 5C). Subsequent to *in vitro* DTNB assay results, evaluation of intracellular GSH depletion across different treatment groups, showed the most notable reduction in green fluorescence intensity, showing efficient GSH depletion by Cu-PB and SRF (Fig. 5D and Supporting Information Fig. S14). The fluorescence-based quantitative assessment detailed above effectively quantified the production of ROS, lipid peroxidation, and GSH depletion associated with ferroptosis. These findings demonstrated that ROS levels in the Cu-PB + SRF (+) group were markedly elevated in comparison to the PB and SRF groups. Regarding lipid peroxidation, both Cu-PB and SRF conditions displayed dominant lipid peroxidation under mild illumination, which was statistically distinct from the control group. Furthermore, as predicted, the Cu-PB + SRF (+) group exhibited the most pronounced GSH depletion, which was also remarkably different from the control group. Additionally, flow cytometry assessed 4T1 cell viability in each group, revealing that the Cu-PB + SRF (+) group experienced a substantial mortality increase (63.6%), significantly surpassing the mortality induced by Cu-PB alone (38.5%) (Fig. 5E and F). In summary, the concerted effects of Cu-PB and SRF facilitated effective ROS and LPO production, GSH depletion, and tumor cell death induction with high efficiency.

3.6. In vivo TNBC treatment via Cu-PB + SRF@MNs

Inspired by the *in vitro* anti-tumor efficacy of Cu-PB + SRF (+), we proceeded to evaluate its anti-tumor potency using *in situ* 4T1 tumor-bearing murine models *in vivo*. To establish a TNBC model, 5×10^5 4T1 cells were inoculated into the right fourth mammary gland of mice (Fig. 6A). Upon tumor volumes reaching 50−80 mm^3, mice were randomly assigned to eight treatment groups, as follows: Control, Control (+), PB + SRF@MNs, Cu-PB@MNs, Cu-PB@MNs (+), SRF@MNs, Cu-PB + SRF@MNs and Cu-PB + SRF@MNs (+). For the groups receiving MN patches, each patch was gently pressed onto the tumor site for 5 min, while mice in the light-activated treatment group were irradiated with NIR laser at 1 W/cm^2 for 5 min after anesthesia, ensuring consistent treatment duration. Concomitantly, an IR thermal imager monitored the tumor site to maintain the temperature below 42 °C ($T \leq 42$ °C) (Fig. 6B and Supporting Information Fig. S15). Tumor progression was evaluated through manual measurements and imaging throughout the treatment period, with analysis revealing that tumors in the Cu-PB + SRF@MNs (+) group exhibited the slowest growth, whereas tumor growth in the remaining treatment groups was variably suppressed (Fig. 6C and D). The body weight in all groups showcased no prominent fluctuations throughout the treatment period (Fig. 6E). This could be attributed to the synergistic enhancement of ferroptosis in tumor cells induced by Cu-PB + SRF@MNs (+) *via* CDT and SRF, facilitated by mild laser irradiation and hyperthermia within the tumor microenvironment. For the biosafety evaluation, a histomorphological examination of the heart, liver, spleen, lung, and kidney in the final treatment group (Cu-PB + SRF@MNs (+)) revealed no noticeable abnormalities (Supporting Information Fig. S16). Furthermore, the Cu-PB + SRF@MNs (+) group exhibited a markedly prolonged survival time compared to other groups (Supporting Information Fig. S17). Routine blood tests and blood biochemistry analyses revealed no significant changes in mice treated with Cu-PB + SRF@MNs (+) (Supporting Information Figs. S18 and S19). Thus, Cu-PB + SRF@MNs (+) demonstrated exceptional biosafety.

Tumor tissue sections were stained for Ki-67, terminal deoxynucleotidyl transferase dUTP nick end labeling (TUNEL), and H&E to assess changes and cell proliferation in the Cu-PB + SRF@MNs (+) group. H&E staining revealed pronounced vacuolization and characteristic cell death in the Cu-PB + SRF@MNs (+) cohort (Fig. 6F). Besides, the Ki-67 and TUNEL assays demonstrated the lowest percentage of Ki-67 positive cells and a higher percentage of TUNEL positive cells compared to other groups, attributed to the co-inductive effect of ferroptosis by Cu-PB and SRF. To elucidate the molecular mechanism underlying the tumor-suppressive effects of Cu-PB + SRF@MNs (+), we evaluated GPX4 expression levels in tumor tissues. The Cu-PB + SRF@MNs (+) treated group exhibited the weakest GPX4 fluorescence intensity compared to other groups, indicating a superior capability of Cu-PB + SRF@MNs (+) to mitigate cellular lipid peroxidation in the 4T1 tumor-bearing mouse model. Overall, the Cu-PB + SRF@MNs (+) group employed the desired "brake release" strategy, achieving optimal therapeutic outcomes *in vivo*. This could be attributed to the cascade action of SRF and Cu ions released from Cu-PB, which enhanced tumor cell sensitivity to ferroptosis by depleting GPX4.

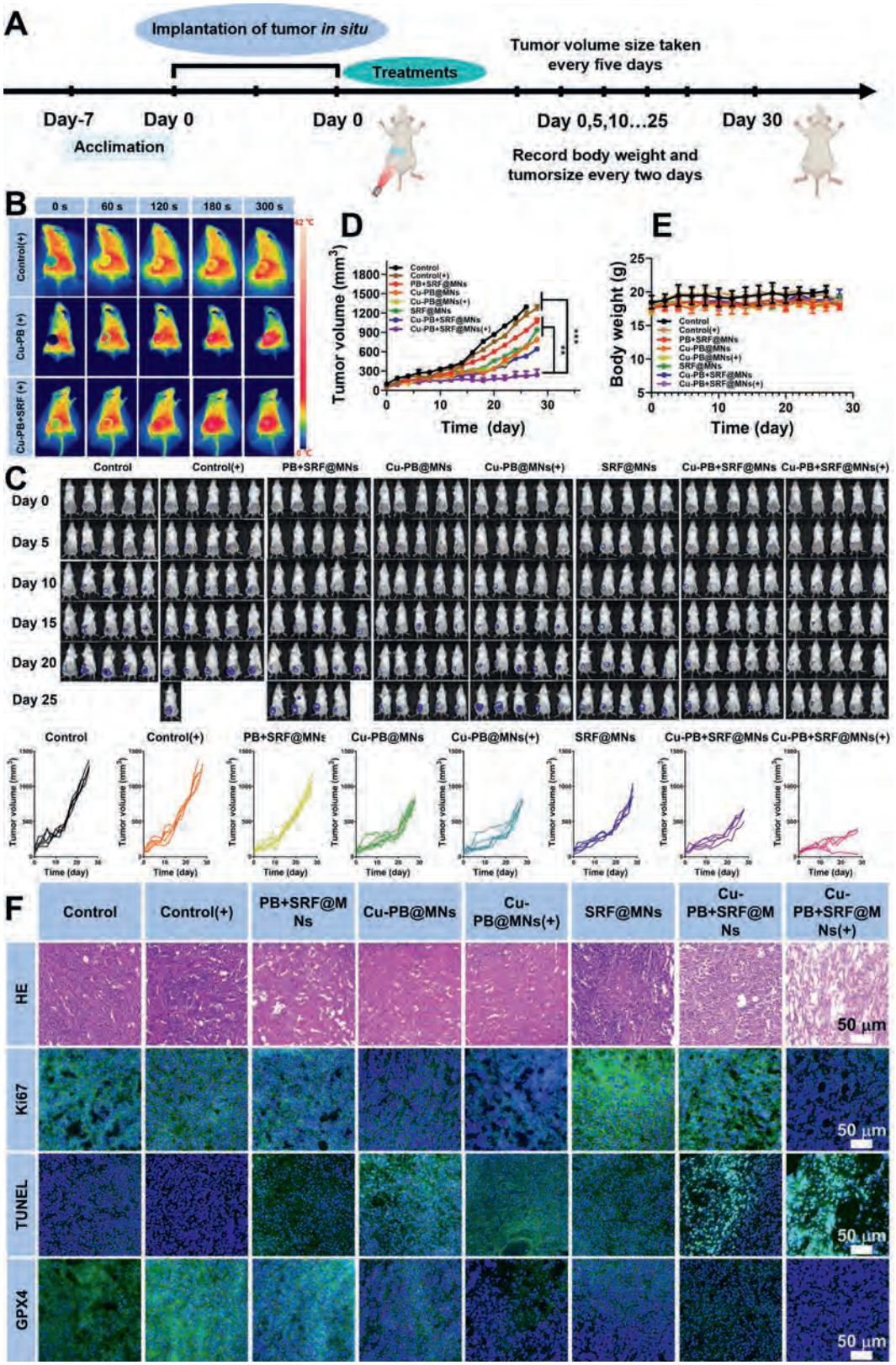

Figure 6 *In vivo* therapeutic efficacy of Cu-PB + SRF in 4T1 orthotopic tumor-bearing mice. (A) Establishment of 4T1 orthotopic tumor mice model and Cu-PB + SRF treatment diagram. (B) IR imaging of mice following exposure to NIR light (808 nm 1 W/cm^2, 5 min). (C) Representative bioluminescence images of 4T1 tumor-bearing mice post various treatments (D) Average tumor growth curves post different treatments. (E) Weight fluctuations across distinct mouse groups. (F) H&E, Ki67, TUNEL, and GPX4 staining of tumor slices in different interventions. Scale bar = 50 μm. Data are presented as mean ± SD (n = 3). $^{**}P < 0.01$, $^{***}P < 0.001$.

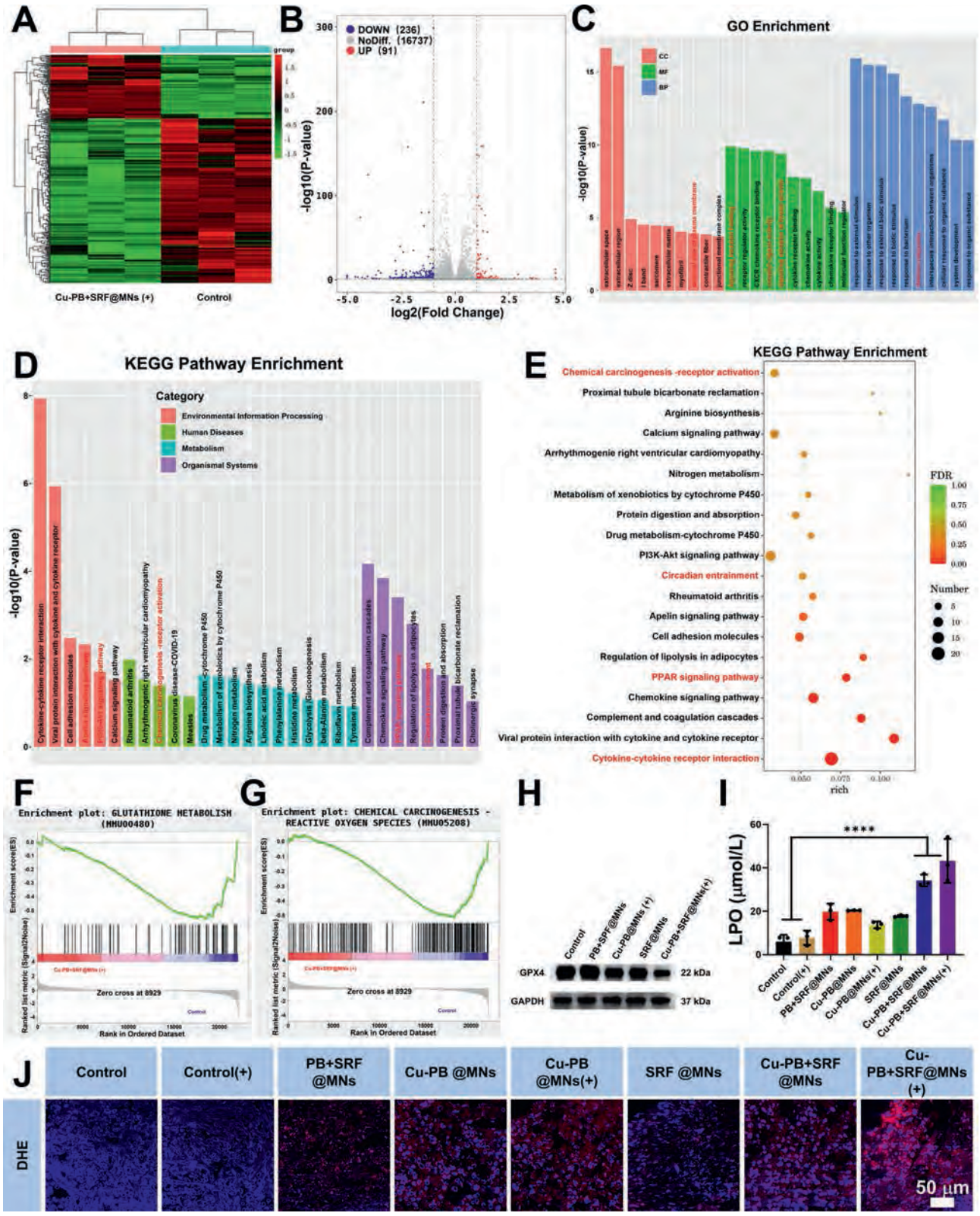

Figure 7 Transcriptome sequencing in tumor tissues. (A) Heat map analysis of DEGs. (B) Volcano plot of DEGs (C) GO enrichment of DEGs. (D, E) KEGG enrichment of DEGs. (F, G) Selected GSEA for tumor tissue ferroptosis. (H) Western blot detection of GPX4 protein expression in tumor tissues under different conditions. (I) LPO levels were detected in tumor tissues after different treatments. (J) CLSM images of ROS levels in tumor tissues detected by DHE in different groups. Scale bar = 50 μm. Data are presented as mean ± SD ($n = 3$). ****$P < 0.0001$.

3.7. Transcriptome sequencing changes of tumor tissue

In order to elucidate the *in vivo* anti-tumor mechanism of Cu-PB + SRF@MNs (+), transcriptome sequencing was employed to analyze the differential mRNA expression between the Cu-PB + SRF@MNs (+) and control groups. As depicted in the volcano plot in Fig. 7A, a substantial disparity in gene interplay was discerned with 91 genes manifesting increased activity and 236 genes displaying decreased activity (Fig. 7B). An evaluation employing bioinformatics was executed through the use of Gene Ontology (GO) and KEGG analyses, identifying the enrichment of specific gene sets in biological processes, cellular components, molecular functions, and relevant metabolic or signaling pathways, with conspicuous pathways exhibiting significant differences highlighted in Fig. 7C and D. KEGG pathway analysis unveiled several pathways, including Apelin, PI3K−Akt, PPAR and circadian rhythm, which were markedly correlated with the ferroptosis induced by Cu-PB + SRF@MNs (+) (Fig. 7E).

Furthermore, GSEA examination recognized distinct modifications in gene expression across an array of biological conditions in the Cu-PB + SRF@MNs (+) groups. The outcomes were disclosed in Fig. 7F and G and in Supporting Information Fig. S20, including ROS, glutathione metabolism, and lipid peroxidation signaling pathways associated with ferroptosis. It has been documented that a reduction in GPX4 activity could provoke cellular death *via* the impairment of oxidative stress. To further validate this, Western blotting analysis of GPX4 protein expression at tumor sites in mice from different treatment groups revealed that SRF alone or the PB + SRF combination had a slight effect while Cu-PB + SRF treatment markedly suppressed GPX4 expression under mild laser exposure (Fig. 7H). To evaluate the levels of deleterious ROS and LPO, an indicator of ferroptosis, DHE immunofluorescence staining and LPO kit assay were conducted on tumor tissues, demonstrating that administration of Cu-PB + SRF@MNs significantly elevated ROS generation and LPO concentration (Fig. 7I and J). These findings collectively substantiate the 'accelerator-pressing' strategy, likely due to the synergistic augmentation of ROS levels by Cu^{2+} and Fe^{3+} liberated from Cu-PB *via* an intensified Fenton/Fenton-like reaction under mild photothermal conditions, clarifying the underlying mechanism for the superior therapeutic efficacy of Cu-PB + SRF@MNs (+) group *in vivo*.

4. Conclusions

In conclusion, this research presents an innovative 'brake-release and accelerator-pressing' strategy by engineering a dissolving hyaluronic acid microneedle patch loaded with Cu-PB and SRF for highly effective TNBC treatment through dual-ferroptosis induction. With the integration of Cu ions, Cu-PB exhibited not only superior photothermal conversion efficiency and ROS catalytic activity but also an enhanced capacity for GSH depletion. The incorporation of Cu-PB and SRF into the microneedles significantly augmented their mechanical robustness, thereby improving skin penetration. Furthermore, the superior solubility from Cu-PB + SRF@MNs ensures complete dissolution under mild photothermal conditions, facilitating the precise and targeted delivery of Cu-PB and SRF to the tumor site. The presence of Cu-PB and SRF disrupted intracellular antioxidant mechanisms, augmenting tumor cell sensitivity to ferroptosis by binding Cu^{2+} to GPX4 and inhibiting the cystine/glutamate antiporter, while also amplifying the production of cytotoxic hydroxyl radicals *via* an intense Fenton/Fenton-like reaction, thereby elevating ROS and LPO levels both i*n vitro* and *in vivo*. These outcomes suggest that this strategy effectively induces ferroptosis in tumor cells, highlighting the substantial potential of this dual-ferroptosis induction microneedle patch for the treatment of drug-resistant TNBC.

Acknowledgments

This work was financially supported by the Research Fund of Anhui Institute of Translational Medicine (2022zhyx-B02, China), the Distinguished Youth of Natural Science Research Projects in Anhui Province Universities (2024AH020005, China), the Anhui Provincial Natural Science Foundation (2208085Y24, China), and Open Project of Key Laboratory of Science and Engineering for the Multi-modal Prevention and Control of Major Chronic Diseases, Ministry of Industry and Information Technology (MCD-2023-1-14, China). Thanks to Shanghai Fudan-Zhangjiang Bio-Pharmaceutical Co., Ltd. for the kind support for microneedle characterization.

Author contributions

Yujie Wang, Zhaoyou Chu, and Peisan Wang designed the experiment, investigated the literature, proposed, and conducted the physical, chemical and biological experiments, and completed the first draft. Tao Li, Yu Jin, Silong Wu, Xiaowei Song, Weinan Zhang, Miaomiao Yang, and Zhengbao Zha supervised the first draft. Haisheng Qian and Yan Ma directed the work.

Conflicts of interest

The authors declare no competing financial interest.

Appendix A. Supporting information

Supporting information to this article can be found online at https://doi.org/10.1016/j.apsb.2025.05.034.

References

1. Yu XR, Li XJ, Chen QW, Wang SY, Xu RZ, He Y, et al. High intensity focused ultrasound-driven nanomotor for effective ferroptosis-immunotherapy of TNBC. *Adv Sci* 2024;**11**:2305546.
2. Waks A, Winer E. Breast cancer treatment a review. *JAMA* 2019;**321**: 288−300.
3. Meng XY, Wu JY, Hu ZF, Zheng XW, Wang ZF. Coordinating effect of ferroptosis and *in situ* disulfiram toxification for enhanced cancer therapy. *Chem Eng J* 2024;**484**:149313.
4. Dixon S, Lemberg K, Lamprecht M, Skouta R, Zaitsev E, Gleason C, et al. Ferroptosis: an iron-dependent form of nonapoptotic cell death. *Cell* 2012;**149**:1060−72.
5. Huang L, Zhu JY, Xiong W, Feng J, Yang JX, Lu XY, et al. Tumor-generated reactive oxygen species storm for high-performance ferroptosis therapy. *ACS Nano* 2023;**17**:11492−506.
6. Zhou LL, Chen JJ, Li RH, Wei LZ, Xiong HT, Wang CH, et al. Metal-polyphenol-network coated Prussian blue nanoparticles for synergistic ferroptosis and apoptosis *via* triggered GPX4 inhibition and concurrent *in situ* bleomycin toxification. *Small (Weinh)* 2021; **17**:2103919.
7. Fu FQ, Wang WH, Wu LJ, Wang WH, Huang ZW, Huang Y, et al. Inhalable biomineralized liposomes for cyclic Ca^{2+}-burst-centered endoplasmic reticulum stress enhanced lung cancer ferroptosis therapy. *ACS Nano* 2023;**17**:5486−502.

8. Yang XH, Sun XX, Lei J, Shi XB, Zhang SW, Luo C. Redox-regulating nanotherapeutics potentiating ferroptosis-driven cancer treatment. *Chem Eng J* 2024;**484**:149518.
9. Wang YN, Calvert A, Cardenas H, Rink J, Nahotko D, Qiang WN, et al. Nanoparticle targeting in chemo-resistant ovarian cancer reveals dual axis of therapeutic vulnerability involving cholesterol uptake and cell redox balance. *Adv Sci* 2024;**11**:2305212.
10. Seibt T, Proneth B, Conrad M. Role of GPX4 in ferroptosis and its pharmacological implication. *Free Radic Biol Med* 2019;**133**:144−52.
11. Li Y, Fan WZ, Gu X, Liu SP, He TT, Gou SQ, et al. Biodegradable ferric phosphate nanocarriers with tumor-specific activation and glutathione depletion for tumor self-enhanced ferroptosis and chemotherapy. *Adv Funct Mater* 2024;**34**:2313540.
12. Wang YM, Wu XR, Ren Z, Li YL, Zou WL, Chen JC, et al. Overcoming cancer chemotherapy resistance by the induction of ferroptosis. *Drug Resist Updates* 2023;**66**:100916.
13. Liu KX, Huang L, Qi SY, Liu SC, Xie WN, Du LY, et al. Ferroptosis: the entanglement between traditional drugs and nanodrugs in tumor therapy. *Adv Healthcare Mater* 2023;**12**:2203085.
14. Dolma S, Lessnick S, Hahn W, Stockwell B. Identification of genotype-selective antitumor agents using synthetic lethal chemical screening in engineered human tumor cells. *Cancer Cell* 2003;**3**:285−96.
15. Zhou TJ, Zhang MM, Liu DM, Huang LL, Yu HQ, Wang Y, et al. Glutathione depletion and dihydroorotate dehydrogenase inhibition actuated ferroptosis-augment to surmount triple-negative breast cancer. *Biomaterials* 2024;**305**:122447.
16. Tang QQ, Wang YY, Yan B, Zhang J, Wang T, Fang Y, et al. Intracellular magnetic hyperthermia sensitizes sorafenib to orthotopic hepatocellular carcinoma *via* amplified ferroptosis. *ACS Nano* 2024;**18**: 29804−19.
17. Wang ZJ, Zhou CY, Zhang YM, Tian XC, Wang HC, Wu JB, et al. From synergy to resistance: navigating the complex relationship between sorafenib and ferroptosis in hepatocellular carcinoma. *Biomed Pharmacother* 2024;**170**:116074.
18. Hou MM, Liu MC, Yu HY, Kou YF, Jia J, Zhou QY, et al. Spatially asymmetric nanoparticles for boosting ferroptosis in tumor therapy. *Nano Lett* 2024;**24**:1284−93.
19. Jiang YC, Jin Y, Feng CC, Wu YY, Zhang WN, Xiao L, et al. Engineering hyaluronic acid microneedles loaded with Mn^{2+} and temozolomide for topical precision therapy of melanoma. *Adv Healthcare Mater* 2024;**13**:2303215.
20. Chen K, Gu L, Zhang QF, Luo Q, Guo SW, Wang B, et al. Injectable alginate hydrogel promotes antitumor immunity through glucose oxidase and Fe^{3+}amplified RSL3-induced ferroptosis. *Carbohydr Polym* 2024;**326**:121643.
21. Wang LY, Tong L, Xiong ZC, Chen Y, Zhang P, Gao Y, et al. Ferroptosis-inducing nanomedicine and targeted short peptide for synergistic treatment of hepatocellular carcinoma. *J Nanobiotechnol* 2024; **22**:533.
22. Lei HL, Pei ZF, Jiang CY, Cheng L. Recent progress of metal-based nanomaterials with anti-tumor biological effects for enhanced cancer therapy. *Explorations* 2023;**3**:20220001.
23. Wang XW, Cheng L. Multifunctional Prussian blue-based nanomaterials: preparation, modification, and theranostic applications. *Coord Chem Rev* 2020;**419**:213393.
24. Ma SN, Li D, Jia XN, Xu WG, Ding GY, He JY, et al. Homologous tumor targeting molybdenum-doped Prussian blue for enhancing immunotherapy via PTT/CDT and remodeled tumor immune microenvironment. *Adv Funct Mater* 2024;**34**:2402692.
25. Wang PF, Sun SH, Bai GS, Zhang RQ, Liang F, Zhang YZ. Nanosized Prussian blue and its analogs for bioimaging and cancer theranostics. *Acta Biomater* 2024;**176**:77−98.
26. Li ZH, Chen Y, Sun YX, Zhang XZ. Platinum-doped Prussian blue nanozymes for multiwavelength bioimaging guided photothermal therapy of tumor and anti-inflammation. *ACS Nano* 2021;**15**:5189−200.
27. Xue Q, Yan D, Chen X, Li XF, Kang R, Klionsky D, et al. Copper-dependent autophagic degradation of GPX4 drives ferroptosis. *Autophagy* 2023;**19**:1982−96.
28. Xie XX, Chen CC, Wang C, Guo YJ, Sun BH, Tian JX, et al. Targeting GPX4-mediated ferroptosis protection sensitizes BRCA1-deficient cancer cells to PARP inhibitors. *Redox Biol* 2024;**76**:103350.
29. Wu WC, Yu LD, Pu YY, Yao HL, Chen Y, Shi JL. Copper-enriched Prussian blue nanomedicine for *in situ* disulfiram toxification and photothermal antitumor amplification. *Adv Mater* 2020;**32**:2000542.
30. Lian H, Guan P, Tan HY, Zhang XS, Meng ZX. Near-infrared light triggered multi-hit therapeutic nanosystem for tumor specific photothermal effect amplified signal pathway regulation and ferroptosis. *Bioact Mater* 2022;**9**:63−76.
31. Zhao JW, Duan W, Liu XY, Xi FN, Wu JM. Microneedle patch integrated with porous silicon confined dual nanozymes for synergistic and hyperthermia-enhanced nanocatalytic ferroptosis treatment of melanoma. *Adv Funct Mater* 2023;**33**:2308183.
32. Feng CC, Zheng W, Jiang YC, Fu WY, Huang WK, Shen CL, et al. Au nanorods activated the Zn/Ce composites with cancer cell specific cytotoxicity for enhanced chemodynamic therapy. *Nano Lett* 2023;**24**: 295−304.
33. Zhang WN, Jiang YC, Liu LT, Shen H, Huang XY, Zheng W, et al. Implantable microneedles loaded with nanoparticles surface engineered escherichia coli for efficient eradication of triple-negative breast cancer stem cells. *Nano Lett* 2025;**25**:2041−51.